Evaluation of Precipitating Hydrometeor Parameterizations in a Single-Moment Bulk Microphysics Scheme for Deep Convective Systems over the Tropical Central Pacific

WOOSUB ROH AND MASAKI SATOH

Atmosphere and Ocean Research Institute, University of Tokyo, Kashiwa-shi, Chiba, Japan

(Manuscript received 14 August 2013, in final form 26 February 2014)

ABSTRACT

Cloud microphysics of deep convective systems over the tropical central Pacific simulated by a cloud system–resolving model using satellite simulators are evaluated in terms of the joint histogram of cloud-top temperature and precipitation echo-top heights. A control experiment shows an underestimation of stratiform precipitation and a higher frequency of precipitating deep clouds with top heights higher than 12 km when compared with data from the Tropical Rainfall Measuring Mission. The comparison shows good agreement for horizontal distribution and statistical cloud size distributions of deep convective systems. Biases in the joint histogram are improved by changing cloud microphysics parameters of a single-moment bulk microphysics scheme. The effects of size distribution of precipitating hydrometeors are examined. Modification of the particle size distributions of rain, snow, and graupel size distributions based on observed relationships improves cloud precipitation statistics. This study implies that a single-moment bulk cloud microphysics scheme can be improved by employing comparison of satellite observations and diagnostic relationships.

1. Introduction

Tropical precipitation systems make important contributions to the global energy budget and play a key role in climate and weather modeling. Representations of tropical precipitation systems by high-resolution nonhydrostatic models, such as cloud system–resolving models (CSRM) without cumulus parameterization, have successfully reproduced realistic structures of cloud systems associated with precipitation, such as the Madden–Julian oscillation (Miura et al. 2007). Nevertheless, deficiencies exist and the numerical simulations continue to be improved.

One important issue in CSRMs is the parameterization of the microphysical processes of hydrometeors. Sophisticated microphysical models, such as bin microphysics, have been developed to express more flexible size distributions and physical processes (Lynn et al. 2005; Iguchi et al. 2008; Khain and Lynn 2009; Suzuki et al. 2010). Bulk microphysics has assumptions about size distributions, such as exponential or gamma distributions, while bin microphysics makes no assumption regarding size distribution, which consists of many bins of a mass or number concentration. However, such schemes require more computational resources for calculations and are thus used primarily for idealized or small-domain experiments rather than for realistic configurations. Bulk microphysics schemes are used to simulate precipitation systems for practical applications.

Bulk microphysics schemes are used to simulate precipitation systems for practical applications and are commonly subdivided into single-moment and multimoment schemes. Single-moment schemes that calculate only the mass concentrations of hydrometeors (e.g., Lin et al. 1983) have been widely used for large-scale experiments and long-term CSRM simulations because of their ease of use and computational efficiency. Double-moment schemes that prognostically calculate both the mass and number concentrations of hydrometeors are currently being developed (Morrison et al. 2005; Seifert and Beheng 2006; Lim and Hong 2010; Seiki and Nakajima 2014). Double-moment schemes can predict changes in hydrometeor number concentration and enable explicit calculation of nucleation processes related to indirect aerosol effects and potentially more consistent treatment of the radiation effects of cloud particles (Seiki et al. 2014).

Denotes Open Access content.

Corresponding author address: Woosub Roh, Atmosphere and Ocean Research Institute, University of Tokyo, 5-1-5, Kashiwanoha, Kashiwa-shi, Chiba, Japan.
E-mail: ws-roh@aori.u-tokyo.ac.jp

DOI: 10.1175/JAS-D-13-0252.1

In addition, double-moment schemes exhibit different characteristics in comparison with single-moment bulk microphysics schemes, for example, the use of a double-moment scheme in idealized cases of squall lines in widespread trailing, a stratiform precipitation region, and different rain evaporation rates (Morrison et al. 2009). Some studies have analyzed where these differences originate or how single-moment bulk schemes can be improved (Thompson et al. 2008; Morrison et al. 2009; Van Weverberg et al. 2012). In addition, Lang et al. (2007, 2011) reduced the biases of the single-moment bulk scheme for simulated radar reflectivities by improving the microphysical processes and size distributions of graupel and snow.

Many efforts have been made toward the evaluation and improvement of microphysics schemes based on in situ aircraft observation data and ground radar observations (Milbrandt et al. 2008; Hong et al. 2010; Molthan et al. 2010). However, ground radar observations and aircraft data have spatial and sampling limits. Recent research has evaluated and investigated this using satellite observation data, such as those from the Tropical Rainfall Measuring Mission (TRMM), *CloudSat*, and *Cloud–Aerosol Lidar and Infrared Pathfinder Satellite Observations* (*CALIPSO*) (Masunaga et al. 2008, 2010; Matsui et al. 2009; Inoue et al. 2010; Satoh et al. 2010; Bodas-Salcedo et al. 2011; Delanoe et al. 2011; Kodama et al. 2012; Hashino et al. 2013). Two approaches are used to evaluate CSRMs using satellite data for the spatial and vertical distributions of cloud systems. One is to directly compare the output data of CSRMs and retrieve physical parameters from satellite data, and the other is to compare radiances in satellite data with simulated radiances from CSRM output data using satellite simulators (Masunaga et al. 2010; Bodas-Salcedo et al. 2011; Hashino et al. 2013). The latter cases are more consistent because we can establish the same microphysical assumptions about hydrometeors, such as their size distributions and density, in the model and the simulators.

Discrepancies between observations and numerical simulations generally arise from both dynamical and physical processes. In this study, we focus on the microphysics aspects mainly, size distributions in single-moment bulk microphysics. Microphysical size distributions are not only related to microphysical processes, such as collection and deposition–evaporation but also have impacts on cloud properties and consequently on radiative transfer, latent heating, and surface precipitation (Li et al. 2008; Luo et al. 2010; Varble et al. 2011). Several studies and sensitivity tests of precipitation systems have been conducted using a single-moment microphysics scheme (Gilmore et al. 2004; Satoh and Matsuda 2009; Van Weverberg et al. 2011; Lang et al. 2011). We investigate and evaluate the parameterization with satellite observation data from TRMM. In addition, we investigate the effects on the simulated radiances by changing the size distribution assumptions and mass–diameter (M–D) relationship.

In this study, we focus on mesoscale convective systems over the tropical central Pacific Ocean region. We investigate the horizontal distribution of cloud sizes, the joint probability distributions of cloud-top temperature, precipitation-top height (PTH), and contoured frequency by altitude diagrams (CFADs) of radar reflectivities for each category using a TRMM precipitation radar (PR) and infrared scanner following the approach proposed by Masunaga and Kummerow (2006) and Matsui et al. (2009).

Several studies have examined the role of microphysics parameterizations in tropical convective systems. Powell et al. (2012) evaluated properties of the continental tropical anvil clouds using six different microphysics schemes [Goddard: Tao et al. (1989) and Lang et al. (2007); State University of New York at Stony Brook–Y. Lin (SBU-YLIN): Lin and Colle (2011); Weather Research and Forecasting (WRF) Double-Moment 6-class (WDM6): Lim and Hong (2010); Thompson: Thompson et al. (2008); Morrison: Morrison et al. (2009); and Milbrandt: Milbrandt and Yau (2005)]. Caine et al. (2013) compared results of numerical simulations with radar observations using two different microphysics schemes [Purdue-Lin: Lin et al. (1983) and Rutledge and Hobbs (1984); and Thompson: Thompson et al. (2008)] through a cell-tracking algorithm and found overestimation of storm heights of convective systems over the tropical ocean. Single-moment bulk microphysics results correspond to previous studies such as less anvil clouds than observations related to larger domain-averaged outgoing longwave radiation (OLR) (Blossey et al. 2007; Zhou et al. 2007) and overestimation of radar reflectivity (Li et al. 2008; Varble et al. 2011). These studies focused on comparisons and evaluations using different microphysics schemes. Since different microphysics schemes are based on different approaches of microphysical processes and size distribution assumptions, it is difficult to interpret why the results are generally different. In this study, we focus on the effects of size distribution parameterizations of precipitating hydrometeors in a simple microphysics scheme on the joint histograms and CFADs of radar reflectivities. We investigate how the results are improved using more realistic size distributions of microphysics.

The remainder of this paper is organized as follows: In section 2, the experimental design and observational

data used in this study are described, and results from a control experiment are introduced and evaluated to show a clear bias of the original scheme. In section 3, we propose several modifications to the hydrometeor size distributions in order to improve the results discussed in section 2. In section 4, the results of sensitivity tests using the modifications proposed in section 3 are presented. Discussion and conclusions are given in sections 5 and 6, respectively.

2. Control experiments and evaluations

a. Experimental design

The Nonhydrostatic Icosahedral Atmospheric Model (NICAM; Tomita and Satoh 2004; Satoh et al. 2008) is a global nonhydrostatic model that can be used as a regional model by transforming the horizontal grid system to focus on a region of interest (the stretched NICAM; Tomita 2008b). In our study, we used the stretched version of NICAM to simulate mesoscale convective systems for a tropical central Pacific region. Because both global and stretched versions of NICAM use the same dynamics and physics schemes, any improvements tested in the stretched NICAM can be directly applied to the global NICAM—an approach proposed by Satoh et al. (2010). We employed this methodology of using stretched NICAM in order to obtain improved simulations over the global domain with high resolution. The target area of this study was over the tropical central Pacific, with its analysis domain of 10°S–10°N, 170°E–170°W and its central point at longitude 180° on the equator. Minimum horizontal grid size was 2.4 km near the central point, and average grid size was approximately 3.3 km, with most of the grids having a size less than 5 km. For the initial data including boundary conditions of sea surface temperature, we used the National Centers for Environmental Prediction Global Data Assimilation System (NCEP 2011). Note that sea surface temperature was kept constant during the integration. In this study, the microphysics scheme used was the NICAM single-moment 6-class bulk scheme (NSW6), which includes water vapor, cloud water, rain, cloud ice, snow, and graupel as hydrometeors (Tomita 2008a). This scheme is based on Lin et al. (1983). The vertical grid number was 40, which covers from the surface to 40-km altitude, and vertical resolutions become coarser toward the upper levels. The integration time starts at 0000 UTC 1 January and terminates at 0000 UTC 1 February 2007. The actual analysis was performed for the period from 0600 UTC 1 January to 0000 UTC 1 February; thus, the 6 h before this analysis can be regarded as the time for the spinup process. We used approximately 1 month of data to obtain more statistical results for mesoscale convective systems for the control experiment (section 2c) and performed a free run without nudging and by not applying the boundary conditions from realistic observations. We obtained mesoscale convective systems in the target area throughout the simulation. Synoptic-scale waves and intraseasonal oscillations are also realistically reproduced in the simulation even after a few days, similar to Miura et al. (2007). The output data are interpolated to 0.0315° (~3.5 km) for comparison with the observation data at the same horizontal grid spacing.

In NSW6, size distributions of precipitating hydrometeors are represented by the simple negative exponential distributions relation

$$n_{[r,s,g]}(D) = N_{0[r,s,g]} \exp(-\lambda_{[r,s,g]} D), \tag{1}$$

where $n(D)$ is the number concentration per unit volume per unit size range, N_0 is an intercept parameter, D is the diameter, and λ is a slope parameter. The subscripts r, s, and g denote rain, snow, and graupel, respectively. The term N_0 is constant in NSW6. The number concentration–weighted mean diameter (i.e., inverse of λ in the exponential distribution; hereafter, mean diameter) is a function of the mass concentration of hydrometeors for a fixed N_0. The M–D relationship for a spherical shape is given by

$$m(D) = \frac{\pi \rho_{[r,s,g]}}{6} D^3, \tag{2}$$

where m is the mass of particles (kg) per unit volume per unit size range, and $\rho_{[r,s,g]}$ is the hydrometeor density. The slope parameter is expressed as

$$\lambda_{[r,s,g]} = \left(\frac{\pi \rho_{[r,s,g]} N_{0[r,s,g]}}{\rho_{\mathrm{air}} q_{[r,s,g]}} \right)^{0.25}, \tag{3}$$

where $q_{[r,s,g]}$ is the hydrometeor mass concentration, and ρ_{air} is the air density.

b. Observational data and satellite forward operators

The infrared equivalent blackbody temperature (TBB) of the *Multi-Functional Transport Satellite* (*MTSAT*) geostationary satellite from the 11-μm infrared channels with 0.04° resolution is used to investigate the cloud-top temperature and the horizontal distribution of cloud systems (Global-IR; Janowiak et al. 2001). The infrared 11-μm TBB from the TRMM 1B01 product and the 13.8-GHz reflectivity and orbital precipitation from TRMM 2A25 are used for the TRMM

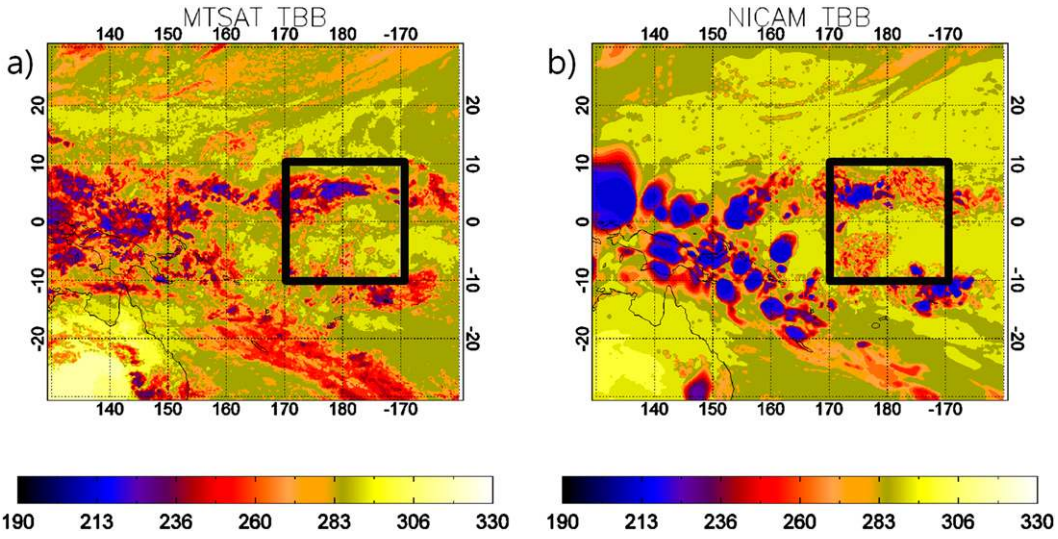

FIG. 1. Comparison of horizontal distribution of TBB (K) from (a) *MTSAT* and the (b) control experiment by NICAM at 0600 UTC 2 Jan 2007. Black box is the analysis domain.

Triple-Sensor Three-Step Evaluation Framework (T3EF) method (Masunaga et al. 2008; Matsui et al. 2009). T3EF involves three steps: 1) obtaining the joint histograms of TBB and PTH, 2) the CFADs of the PR reflectivities, and 3) the cumulative probability distribution of the TRMM Microwave Imager (TMI) 85-GHz brightness temperatures (Masunaga and Kummerow 2006; Matsui et al. 2009). The PTH is identified as the highest altitude of the layer above 17 dBZ of PR reflectivity. The TBB on the PR instantaneous field of view is used, and every data point is interpolated to 0.0315° (~3.5 km) of the horizontal spacing for comparison with the NICAM data.

We use the Satellite Data Simulator Unit (SDSU; Masunaga et al. 2010), version 2.1.4, to compare the radiances of the observation data with those of the NICAM data. In SDSU, the extinction and scattering properties of hydrometeors are calculated on the basis of the Mie theory. These radiative properties are used for calculation of satellite radiances by microwave, radar, and visible–infrared simulators. Snow and graupel are assumed as soft mixtures of air and ice by the Maxwell–Garnett approach (Maxwell-Garnett 1904), which was generalized by Bohren and Battan (1982). The effective dielectric constant of the solid precipitating hydrometer is as follows:

$$\epsilon_{[s,g]} = \frac{(1-f)\epsilon_{\rm ice} + f\gamma\epsilon_{\rm air}}{1-f+f\gamma}, \tag{4}$$

$$\gamma = \left(\frac{2\epsilon_{\rm ice}}{\epsilon_{\rm air}-\epsilon_{\rm ice}}\right)\left[\left(\frac{\epsilon_{\rm air}}{\epsilon_{\rm air}-\epsilon_{\rm ice}}\right)\ln\left(\frac{\epsilon_{\rm air}}{\epsilon_{\rm ice}}\right)-1\right], \tag{5}$$

$$f = 1 - \frac{\rho_{[s,g]}}{\rho_{\rm ice}}, \tag{6}$$

where $\epsilon_{[s,g]}$, $\epsilon_{\rm ice}$, and $\epsilon_{\rm air}$ are the complex dielectric constant of the hydrometer, pure ice, and air, respectively, and f is the volume fraction of ice and air.

We use the same assumed size distributions for rain, snow, and graupel in NICAM and the SDSU. For cloud water and cloud ice, we use the size distributions used in the SDSU because NSW6 has no assumption about the size distributions of cloud ice and cloud water; that is, we set 30 μm as the effective radius of cloud ice and a log-normal distribution of cloud water (the median diameter is 20 μm and the dispersion is 0.35) in the radar simulator and the visible–infrared channel simulator of the SDSU.

c. Results of the control experiment

Figure 1 shows the horizontal distribution of TBB observed by MTSAT and simulated by the stretched NICAM over 30°S–30°N, 130°E–160°W at 0600 UTC 2 January 2007. Two convective bands over the analysis domain (enclosed by the rectangle in Fig. 1) are reproduced well at approximately the same location in MTSAT. One convective system is at approximately 5°N, and the other is in the relatively cloud-populated areas in the southwestern domain (5–10°S, 170°E–180°). In the region outside the rectangle, the horizontal resolutions are coarser than that of the analysis domain; thus, the simulated TBB in coarser resolutions that produce the larger deep clouds than finer resolutions is lower than the observations. The cloud sizes of convective systems seem to be overestimated in the area of

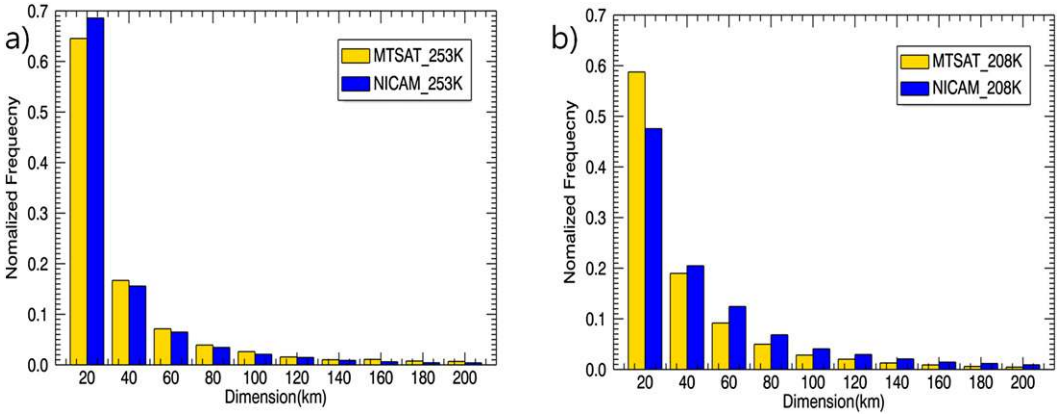

FIG. 2. Histogram of cloud size of TBB defined by the threshold values of (a) 208 and (b) 253 K calculated from 30-day data. Size on abscissa is defined as the square root of the area.

coarse resolution; however, we do not use the coarser resolution region for analysis.

First, to show the statistical behaviors of clouds in the analysis domain, we analyze the size distributions of the upper clouds using the two threshold values of the TBB, 208 and 253 K, following Inoue et al. (2008). We calculated the 30-day 11-μm TBB from vertical profiles of the NICAM simulation snapshot data using the infrared satellite simulator embedded in the SDSU and directly compared the observed and simulated 11-μm TBBs. This is in contrast to the work of Inoue et al. (2008), who compared the observed TBB and the OLR of the NICAM simulations using their respective threshold values. Figure 2a shows that the simulated cold clouds having a threshold of 253 K are similar to those of the observation. The cloud size probability distribution of the deep convective core (208 K) shows that the simulation has larger convective-core fraction than the observation (Fig. 2b). These results are compatible with those of the global NICAM with a 3.5-km horizontal mesh reported by Inoue et al. (2008).

Next, we analyze the vertical properties of precipitating clouds using the T3EF method. In this study, we focus on the joint histograms and CFADs. Matsui et al. (2009) classified cloud types into four categories according to the domain within the joint histogram: shallow, congestus, midcold, and deep clouds (Table 1). Because the different cloud types have different dynamical processes and environmental conditions, it is important to evaluate the quantitative properties of clouds by classifying them into different types. This type of classification method is advantageous for comparison of observations and CSRM output.

Figure 3 shows the joint TBB and PTH histograms from both the simulation and the TRMM observation calculated from 30-day data. Following Masunaga and Kummerow (2006) and Matsui et al. (2009), we use the joint TBB and PTH histograms to classify the cloud types into the four categories given above. In this study, the simulation is targeted on the region of active deep clouds in the tropics, and the populations of deep and midcold clouds are larger than those of shallow and congestus clouds; this characteristic is similar to the Kwajalein Experiment (KWAJEX) case reported by Matsui et al. (2009, their Fig. 2a). For the observation, the percentages of each cloud type are 16.1%, 14.3%, 29.9%, and 21.1% for shallow, congestus, midcold, and deep clouds, respectively. In this case, the midcold clouds are the most populated category, and deep clouds are the second. Deep clouds represent both mesoscale deep convective systems and stratiform clouds. The midcold clouds are primarily related to the stratiform precipitation systems and cirrus partially overlapped congestus according to the TRMM PR convective–stratiform classification data.

For the simulation shown in the right panel of Fig. 3, the percentages of each cloud type are 23.5%, 11.7%, 17.4%, and 32.0% for shallow, congestus, midcold, and deep clouds, respectively. It is clear that the simulation produces too many deep clouds and does not represent sufficient stratiform clouds (midcold). This cannot be inferred from the upper-cloud size statistics shown in Fig. 2; thus, we must analyze the vertical structures of the clouds in more detail using the T3EF method. The

TABLE 1. Categorization of cloud types based on the T3EF method (Matsui et al. 2009).

	Shallow	Congestus	Midcold	Deep
TBB (K)	>260	>245	<245	<245
PTH (km)	<4	4–7	4–7	>7

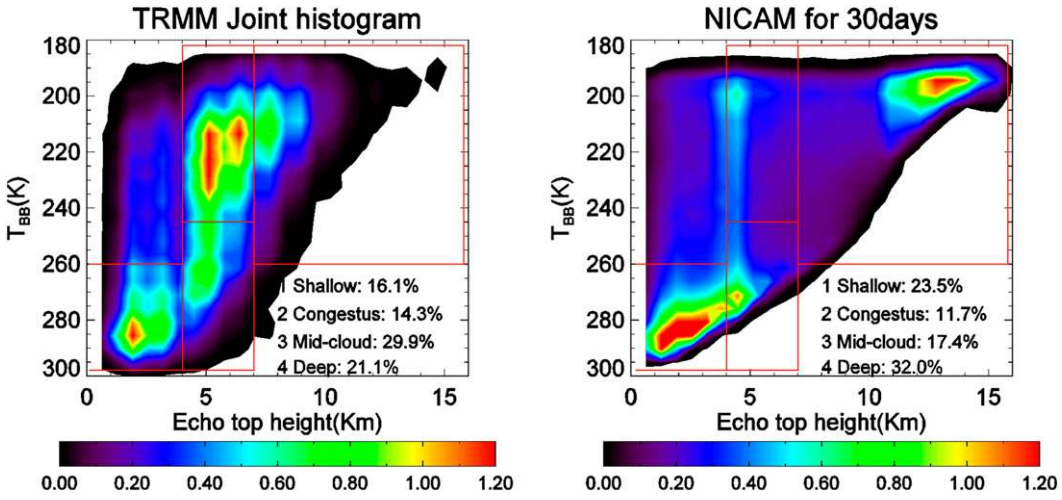

FIG. 3. Joint histograms of PTH and TBB from (a) TRMM and the (b) control experiment calculated from 30-day data during January 2007. The unit of the color bar is % $km^{-1} K^{-1}$.

shallow precipitation is overestimated in comparison with the observation. This means that the control result underestimates stratiform precipitation systems compared with convective precipitation systems.

Figure 3 shows a clear discrepancy in the simulation, that is, high frequencies of PTH near 14 km and low frequencies of PTH between 5 and 10 km. Three discrete distributions appear in the joint histogram of the numerical results at low, medium, and high PTH. By switching off the contribution of each category of hydrometeors in the SDSU, we found that the heavier population near 14 km in PTH is related to the radar reflectivities of the snow category (not shown). The radar reflectivity is calculated from the hydrometeor content and the size distribution assumption in the single-moment bulk microphysics. Thus, one possible reason is overestimation of the mass concentration of snow, and the other is excessively large snow particles over the upper part of the troposphere. We speculate that these discrepancies arise from the incorrect size distributions of precipitating hydrometeors. Two hypotheses will be further investigated in the next section.

Figure 4 shows the CFADs of radar reflectivities of the four cloud types in the T3EF calculated from 30-day data in the tropical central Pacific. In the shallow and congestus clouds, the observed average reflectivity in CFADs increases from upper altitudes to the surface, and the reflectivity is broadly distributed down to the surface (Figs. 4a,c). The CFADs of the simulated congestus and midcold clouds are somewhat similar to those of the observed clouds (Figs. 4c–f); however, they show overestimation of radar reflectivity below 5-km altitude. The modal radar reflectivity in the simulated shallow precipitation does not increase to the surface and is slightly underestimated compared to the observation (Fig. 4b). The simulated congestus precipitation is similar to the observed pattern, and the average radar reflectivity in the CFADs increases toward the surface (Fig. 4d). The observed midcold clouds have a clear bright band near the melting layer (5 km), where the radar reflectivity increases slightly in the observation (Fig. 4e). However, the simulation does not have a clear deviating signal near the melting layer (Fig. 4f; it should be mentioned that the bright band option of the SDSU is not used in this simulation). The CFADs of deep clouds from 10 to 15 km appear similar in the observation and the simulation (Figs. 4g,h); however, they differ from the surface to 10 km, and the radar reflectivities' distribution is broader in the simulations than in the observations. Graupel is found to dominate from 5 to 10 km in the simulation (not shown), which produces stronger signals from deep clouds (Fig. 4h).

3. Modifications of microphysics scheme

In the previous section, we showed the biases of the control experiment using the T3EF analysis of the joint histogram and CFADs, especially for deep clouds. We try to improve these results by modifying the cloud microphysics scheme and focusing on hydrometeor size distribution. We use NSW6 (Tomita 2008a) discussed in section 2c. In the following, we continue to use the single-moment scheme and examine whether the biases are reduced if the available diagnostic relations are applied to the hydrometeor distributions. We describe modifications of the size distributions of snow, graupel, and rain in sections 3b–d, respectively. Sensitivity experiments of these size distribution modifications of

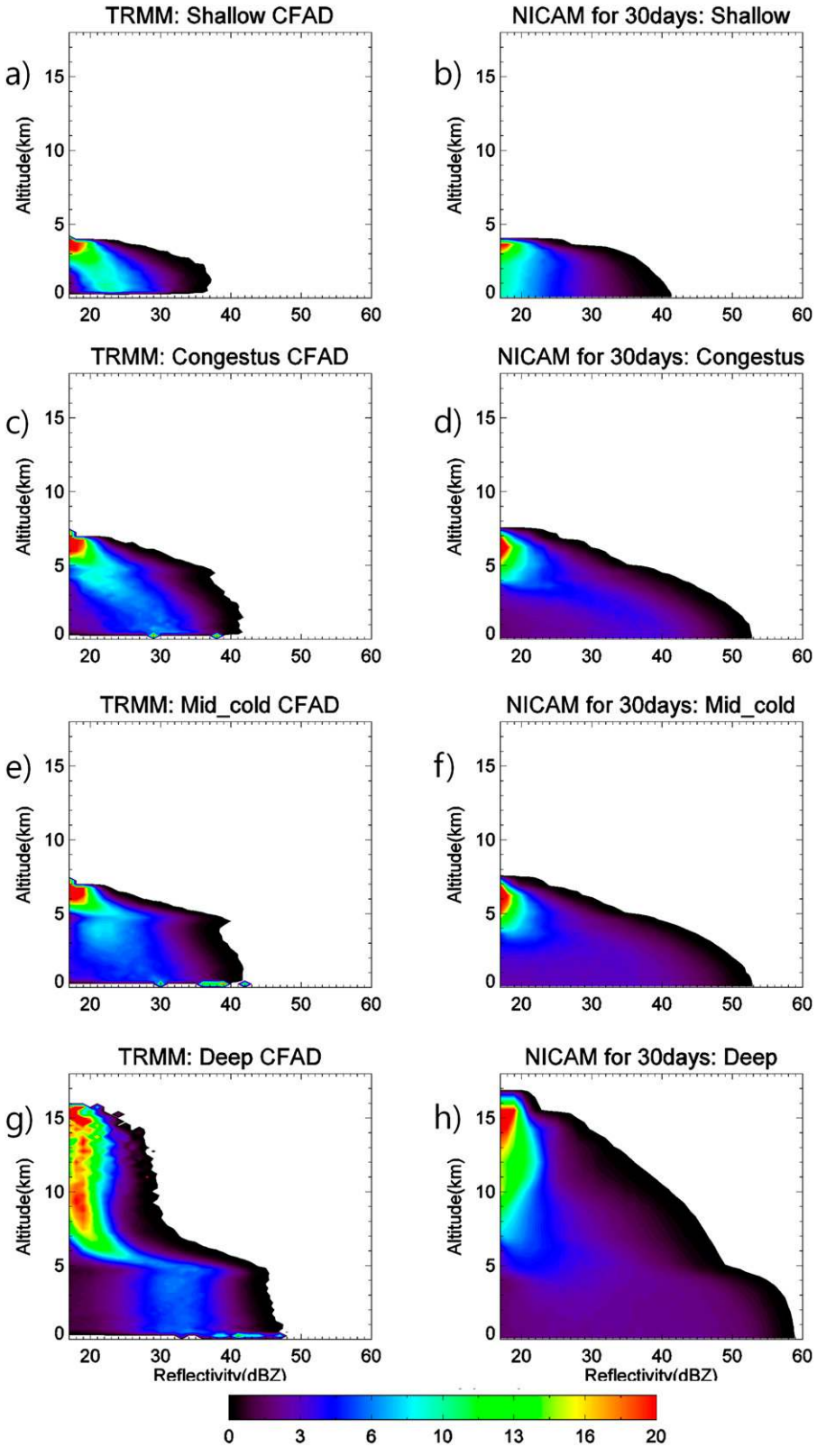

FIG. 4. CFADs for cloud categories of (a),(b) shallow, (c),(d) congestus, (e),(f) midcold, and (g),(h) deep clouds for (left) TRMM observation and the (right) control experiment. The unit of the color bar is % km^{-1} dBZ^{-1}.

snow, graupel, and rain are discussed in sections 4c–e, respectively.

a. Sensitivity to graupel growth and ice nucleation

Before discussing the modifications of the size distributions, we introduce common modifications applied to the original NSW6. One of the well-known problems in single-moment bulk microphysics schemes is overestimation of high-density ice, such as graupel or hail in mesoscale convective systems, compared with observations (Lang et al. 2007; Stith et al. 2002). As the first change in the original scheme, following Lang et al. (2007), we turn off the accretion of snow and cloud ice by graupel [production of graupel by collecting snow (PGACS) and production of graupel by collecting ice (PGACI) in Tomita (2008b)] to reduce the unrealistic presence of high-density ice in the anvil and stratiform portions of clouds. As the second change, we explicitly calculate the ice nucleation and ice deposition processes following Hong et al. (2004) rather than the saturation adjustment of the original NSW6. When we used the saturation adjustment for sensitivity tests of snow and graupel having large $N_{0[s,g]}$, the amount of cloud ice was significantly reduced in the convective core by depositional processes of snow and graupel.

b. Snow

The high frequency of signals above 12 km in PTH in the simulation (Fig. 3) is related to the snow category of the control experiment. We focus on the dependency on the size distribution of snow and examine the changes in the PTH bias with the same size distributions of the other hydrometeors. For the default setting of NSW6, the intercept parameter of snow is set at a constant value, $N_{0s} = 3.0 \times 10^6\,\mathrm{m}^{-4}$, which is based on a ground observation (Gunn and Marshall 1958). However, according to airplane observations, the intercept parameter in the upper troposphere is much larger. For example, Heymsfield et al. (2008) suggest a value of $1.0 \times 10^8\,\mathrm{m}^{-4}$ based on upper-tropospheric aircraft observations.

The size distribution of snow is known to depend on the temperature and results from aggregation and depositional growth processes. Houze et al. (1979, hereafter HZ79) found that N_{0s} depends on the temperature. Some parameterizations used the following temperature dependence for N_{0s} (Hong et al. 2004):

$$N_{0s} = 2.0 \times 10^6 \exp[-0.12 \times (T - T_0)], \tag{7}$$

where $T_0 = 273.15$ K, and T is the ambient temperature (K).

Field et al. (2005, hereafter FS05) introduced a parameterization for the moments of the snow size distribution using a second moment and the temperature based on aircraft observation data. Thompson et al. (2008) implemented this approach in their microphysics scheme and tested it for an idealized case. This parameterization employs the bimodal size distribution using a combination of exponential and gamma distributions:

$$N(D) = M_i^{(j+1)/(j-i)} M_j^{(i+1)/(i-j)} \phi_{ij}(x), \tag{8}$$

where

$$x = D(M_i/M_j)^{1/(j-i)}, \tag{9}$$

$$M_n = \int_0^\infty D^n N(D)\, dD, \tag{10}$$

using the second ($i = 2$) and third ($j = 3$) moments in Table 2 of FS05,

$$\phi_{2,3}(x) = 490.6 \exp(-20.78x) + 17.46x^{0.6357} \exp(-3.290x). \tag{11}$$

After inserting Eqs. (9), (10), and (11) into Eq. (8), the final form of the size distribution is given by

$$N(D) = \frac{M_2^4}{M_3^3} 490.6 \exp(-20.78x_{23}) + 17.46x_{23}^{0.6357} \exp(-3.290x_{23}), \tag{12}$$

where

$$x_{23} = D\frac{M_2}{M_3}. \tag{13}$$

Snow is generally less dense than bulk ice in observations and model assumptions due to the open shapes of snowflakes. The density of snow is known to affect radar reflectivity (Matrosov 1992).

In the default assumption, the density of snow is constant, and the M–D relationship is proportional to the third power of D. Observational studies show that the exponent is closer to 2 than to 3 (Locatelli and Hobbs 1974). The density of snow is inversely proportional to the diameter in several observations. In this study, we adopt the size–density relationship of the spherical shape assumption corresponding to the M–D relationship. Thompson et al. (2008) conducted a similar experiment using an M–D relationship (EXP1; Thompson et al. 2008), where $m(D) = 0.069D^2$ and $\rho_s = 0.13D^{-1}$. We use the empirical equation of Fabry and Szyrmer (1999), given by

TABLE 2. Sensitivity experiments.

	Experiment	Description	Period (days)	Section
	Control	NSW6	30	2
	CON	NSW6	7	
	CON2	PGACI and PGACS are turned off (Lang et al. 2007).	7	3a
		Ice nucleation, ice deposition (Hong et al. 2004).		4b
Snow	Fixed_N0S	$N_{0s} = 3.0 \times 10^6\,\mathrm{m}^{-4}$, $\rho_s = 100\,\mathrm{kg\,m}^{-3}$	7	3b
	HZ79_M3	$N_{0s} = 2.0 \times 10^6 \exp[-0.12 \times (T - T_0)]\,\mathrm{m}^{-4}$, $\rho_s = 100\,\mathrm{kg\,m}^{-3}$		4b
	HZ79_M2	$N_{0s} = 2.0 \times 10^6 \exp[-0.12 \times (T - T_0)]\,\mathrm{m}^{-4}$, $\rho_g = 0.15D^{-1}\,\mathrm{kg\,m}^{-3}$		
	FS05_M2	Bimodal size distribution, $\rho_g = 0.15D^{-1}\,\mathrm{kg\,m}^{-3}$		
Graupel	G1	$N_{0g} = 4.0 \times 10^6\,\mathrm{m}^{-4}$, $\rho_g = 400\,\mathrm{kg\,m}^{-3}$	7	3a
	G100	$N_{0g} = 4.0 \times 10^8\,\mathrm{m}^{-4}$, $\rho_g = 400\,\mathrm{kg\,m}^{-3}$		4a
	LG1	$N_{0g} = 4.0 \times 10^6\,\mathrm{m}^{-4}$, $\rho_g = 33.7\,\mathrm{D}^{-0.3}\,\mathrm{kg\,m}^{-3}$		
	LG100	$N_{0g} = 4.0 \times 10^8\,\mathrm{m}^{-4}$, $\rho_g = 33.7\,\mathrm{D}^{-0.3}\,\mathrm{kg\,m}^{-3}$		
Rain	MP	$N_{0g} = 8.0 \times 10^6\,\mathrm{m}^{-4}$	7	3d
	ZH08	$N_{0r} = 7.106 \times 10^7 \times (10^3 \times \mathrm{LWC})^{0.648}\,\mathrm{m}^{-4}$		4d
	Combined	Over $0.001\,\mathrm{g\,m}^{-3}$ of IWC of snow and graupel in melting layer (highest vertical grid over 0°C) and below $1\,\mathrm{m\,s}^{-1}$ of vertical wind of each grid: $N_{0r} = 7.106 \times 10^7 \times (10^3 \times \mathrm{LWC})^{0.648}\,\mathrm{m}^{-4}$ the other conditions: $8.0 \times 10^6\,\mathrm{m}^{-4}$.		

$$\rho_s = 0.15D^{-1}. \tag{14}$$

We obtain an *M–D* relationship similar to the observations when we insert Eq. (14) into Eq. (2):

$$m(D) = 0.0785D^2. \tag{15}$$

FS05 also used $m(D) = 0.069D^2$ for the second moment of the size distributions in their parameterization. In this study, we used Eq. (15) for FS05 for the sensitivity test.

The effective density is related to the shape of the snow. Larger particles have lower density because they tend to have a two-dimensional planar shape. Smaller precipitation particles have higher densities with a three-dimensional shape.

The default snow size distribution of NSW6 is based on ground observations and does not consider the effect of snow aggregation in the upper troposphere. Thus, it generally overestimates the radar reflectivities of snow. There are several parameterizations of the bulk size distribution of snow, such as HZ79 and FS05. In the control run, the snow mass is proportional to the third order of the mean diameter, whereas it is proportional to approximately the second order in the observations. In section 4c, we test the effects of several parameterizations of snow size distribution and the *M–D* relationship of snow about HZ79 and FS05 given in Table 2 on the joint histogram and CFADs of mesoscale convective systems.

c. Graupel

There are fewer observations of the size distributions of graupel than of snow. The duration of precipitation is known to increase as the intercept parameter of graupel N_{0g} increases (Gilmore et al. 2004; Van Weverberg et al. 2011).

There are large variances in the density of graupel and N_{0g}. We tested an *M–D* relationship for lump graupel in Locatelli and Hobbs (1974):

$$m(D) = 17.6D^{2.7}. \tag{16}$$

We perform sensitivity tests of N_{0g} following Van Weverberg et al. (2011) using Eq. (16) and a higher N_{0g}.

d. Rain

The size distributions of rain in observed convective and stratiform precipitation are known to differ (e.g., Tokay and Short 1996; Maki et al. 2001; Rao et al. 2001). The dominant physical processes related to the size distributions of rain are autoconversion, coalescence, and breakup by positive buoyancy and convergence in convective precipitation, whereas rain originating from the melting of snow or graupel and the evaporation process are more important in stratiform precipitation because the relative humidity is lower than in the convective core. The modal diameters of rain in convective precipitation are smaller than those in stratiform precipitation for the same liquid water content (LWC) (Tokay and Short 1996). Tokay and Short (1996) found that the linear relationship between the LWC and radar reflectivity is different in convective and stratiform precipitation (Fig. 5). In the original NSW6 scheme, the default value of the intercept parameter of rain is fixed at $N_{0r} = 8.0 \times 10^6\,\mathrm{m}^{-4}$. Zhang et al. (2008, hereafter ZH08) introduced the intercept parameter as a function of the LWC based on video disdrometer observations:

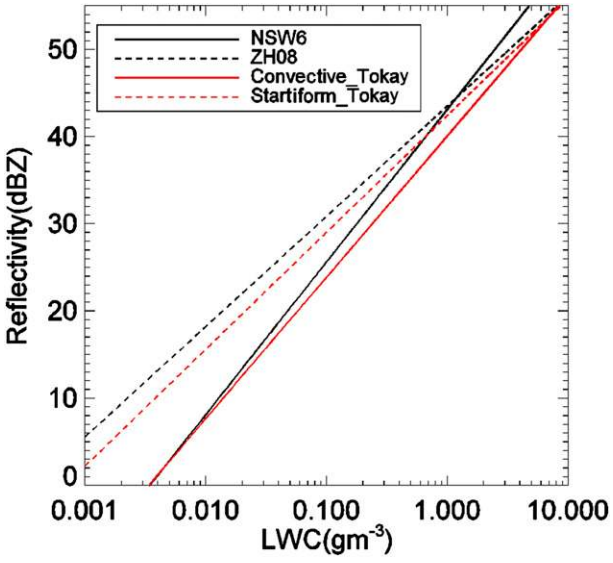

FIG. 5. Relationship between radar reflectivity and LWC for NSW6, ZH08, and observations of convective and stratiform systems from Tokay and Short (1996).

$$N_{0r} = 7.106 \times 10^6 (10^3 \times \mathrm{LWC})^{0.648}. \qquad (17)$$

The term N_{0r} affects other physical processes, such as deposition–evaporation and collection.

Figure 5 compares the relations between the radar reflectivity and LWC calculated from the size distributions used by NSW6 and ZH08 and the corresponding linear experimental fittings for convective and stratiform precipitation derived from the observation of Tokay and Short (1996). The ZH08 parameterization is closer to the observed relationship for stratiform precipitation. The Marshall–Palmer (MP) relation (Marshall and Palmer 1948) is similar to that observed for convective precipitation.

One of the dominant processes related to rain in stratiform precipitation is evaporation. The MP relation is known to lead to overestimation of evaporation in stratiform precipitation because the evaporation process is more active for smaller particles and is sensitive to the particle size of rain (Morrison et al. 2009; Li et al. 2009).

The bulk size distributions of rain in convective and stratiform precipitation are different. The MP relation holds well for convective precipitation, whereas the diagnostic relation of ZH08 performs better for stratiform precipitation when we compare it with the observation of Tokay and Short (1996). One reason is that the MP relation with fixed N_{0r} does not represent the change in mean diameter during evaporation. We introduce a combination of the MP relation and ZH08 method (Combined) in the sensitivity tests. Combined is introduced as follows: 1) we classify the stratiform precipitation region as the region that satisfies the conditions ice water content (IWC) greater than $0.001\,\mathrm{g\,m^{-3}}$ in the melting layer (the highest vertical grid above 0°C) and vertical velocity less than $1\,\mathrm{m\,s^{-1}}$; and 2) the ZH08 method is used to obtain the rain size distribution in the stratiform precipitation region, and the MP relation is used in the convective precipitation region. In section 4e, we will investigate the effect of the rain size distributions of the MP relation, ZH08, and Combined on the joint histogram.

4. Results of sensitivity experiments

a. Sensitivity experiments setup

We perform numerical experiments to examine the sensitivity of the statistics of clouds and precipitation for a 7-day integration time. In this section, the integration time is limited to 7 days, from 1800 UTC 1 January to 1800 UTC 8 January, because we found that the statistics of 7-day integration exhibit a joint histogram and CFADs similar to those of 1-month integration. However, the shallow precipitation is more dominant in this experiment (Fig. 6). Hereafter, we refer to the 7-day integration with the original scheme as CON.

We investigate the impact of various size distribution parameterizations of precipitating hydrometeors on the joint histogram of TBB and PTH. For the modifications of the size distributions, we examine the size distribution of snow (section 4c), then test that of graupel (section 4d), and finally examine that of rain (section 4e). The following experiments adopt the same microphysical framework introduced to CON2 (see below). We summarize all the experiments in Table 2 for the sensitivity tests.

b. Sensitivity to graupel growth and ice nucleation

Before presenting the sensitivities of the size distribution parameterizations of rain, snow, and graupel presented in the previous section, we introduce two changes in the original NSW6 scheme: the neglect of accretion processes of graupel by snow and ice and implementations of ice nucleation and deposition, which are used in all of the following experiments. This experiment is referred to as CON2.

The structure of the joint histogram when these two modifications are applied is similar to the biases of CON. There are high frequencies above 12 km and underestimation of the midcold clouds. The ratio of deep clouds is significantly increased to more than 30% compared to CON (Fig. 6). It means the increase of snow amount and stratiform precipitations makes high

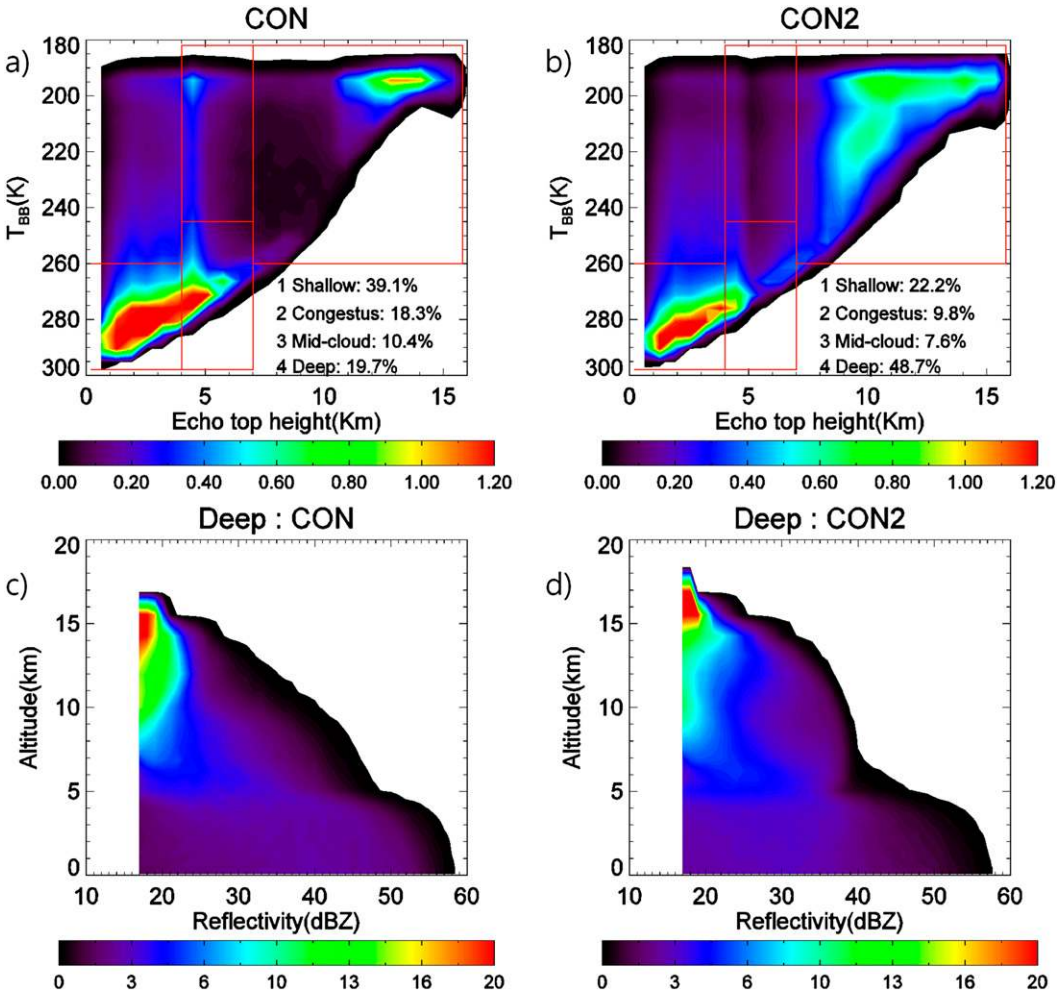

FIG. 6. (a) Joint histogram of PTH and TBB and (c) CFAD of deep clouds in the control experiment for the 7-day simulation and (b) joint histogram and (d) CFAD of deep clouds for the experiment that applied the two modifications to turn off accretion of graupel with snow and ice and used ice nucleation and ice deposition, following Hong et al. (2004) instead of the saturation adjustment.

frequencies in deep clouds with no change of snow size distributions than CON. The average radar reflectivity of CON2 in CFADs is larger above 10-km altitude and smaller between 5 and 10 km than that in CON. The maximum radar reflectivities of CON2 are slightly reduced compared to CON.

c. *Sensitivity to snow size distributions*

Figure 7 shows the probability distribution of PTH in deep clouds at altitudes between 7 and 16 km. A peak appears above 8 km in CON and CON2, whereas the observed peak is located at approximately 8 km in TRMM, which is consistent with Figs. 3 and 6. The parameterizations of the snow size distribution introduced in section 3a reproduce the PTH profiles better than CON. The peak is located near 8.5 km for both the HZ79 and FS05 parameterizations. FS05 show a rapid decrease in the ratio above 10 km, similar to the observation. HZ79 overestimates the frequencies of PTH above 10 km. In addition, the M–D relationship is less sensitive to the PTH distribution.

Figure 8 compares the vertical profiles of the average and maximum radar reflectivity in deep clouds for the sensitivity experiments with each size distribution of snow. The M–D relationship affects the average radar reflectivity profile; the second order of the M–D relationship ($\sim D^2$) using Eq. (15) in the experiments (HZ79_M2) shows lower radar reflectivities than the third order of the M–D relationship ($\sim D^3$) using a fixed density (HZ79_M3). The observed mean radar reflectivity increases sharply from 8 down to 5 km. FS05 reproduces vertical profiles similar to the observed profile. The radar reflectivity of HZ79 is higher than the observed values below 11 km, and it increases from 12 to

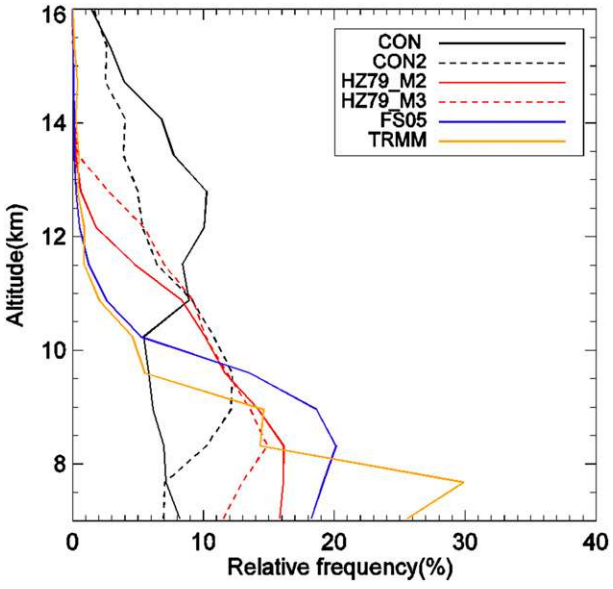

FIG. 7. Comparison of vertical distributions of PTH for parameterizations of snow size distribution. Size distribution assumptions of other precipitating hydrometers are the same in NSW6.

5 km. Thus, FS05 shows better results than HZ79 for the joint histogram and CFADs of deep clouds.

Figure 9 shows the mass spectrum of snow for the mass concentration of snow, 0.1 g m^{-3}, at −10° and −30°C. HZ79 and FS05 show the change of size distribution depends on temperature even for the same ice water content. It reduces the frequency above 12 km in the joint histograms. HZ79_M2 has smaller diameters and radar reflectivity than HZ79_M3. FS05 has the bimodal size distribution and the second order of the *M–D* relationship. These two effects make a more realistic joint histogram and CFADs of deep clouds than HZ79_M3.

It should be noted that these results correspond to previous studies. Using the Thompson parameterization including FS05, Caine et al. (2013) reproduced more realistic storm height distributions than the Lin-type microphysics scheme. Van Weverberg et al. (2013) have also shown that mesoscale convective system (MCS) cloud properties were better captured using the Thompson parameterization.

In conclusion, among the above parameterizations, FS05 performed the best. Therefore, we will use the FS05 parameterization for the snow size distribution in the following experiments.

d. Sensitivity to graupel size distribution

We examine the sensitivity of the graupel size distribution to the snow size distribution as specified in FS05. Table 2 lists the sensitivity experiments on the size distribution of graupel. We test the sensitivity of N_{0g} and the *M–D* relationship. First, we increase N_{0g} from the default value $4.0 \times 10^6\,\mathrm{m}^{-4}$ (G1) to $4.0 \times 10^8\,\mathrm{m}^{-4}$ (G100) based on Knight et al. (1982). We also test the *M–D* relationships for lump graupel in Locatelli and Hobbs (1974) introduced in section 4c with $N_{0g} = 4.0 \times 10^6\,\mathrm{m}^{-4}$ (LG1). Finally, we test the *M–D* relationship of lump graupel with the increased $N_{0g} = 4.0 \times 10^8\,\mathrm{m}^{-4}$ (LG100). The results show only a small sensitivity of the PTH distribution to the graupel size distribution (not shown). However, we found that the graupel size distribution significantly affects the average and maximum

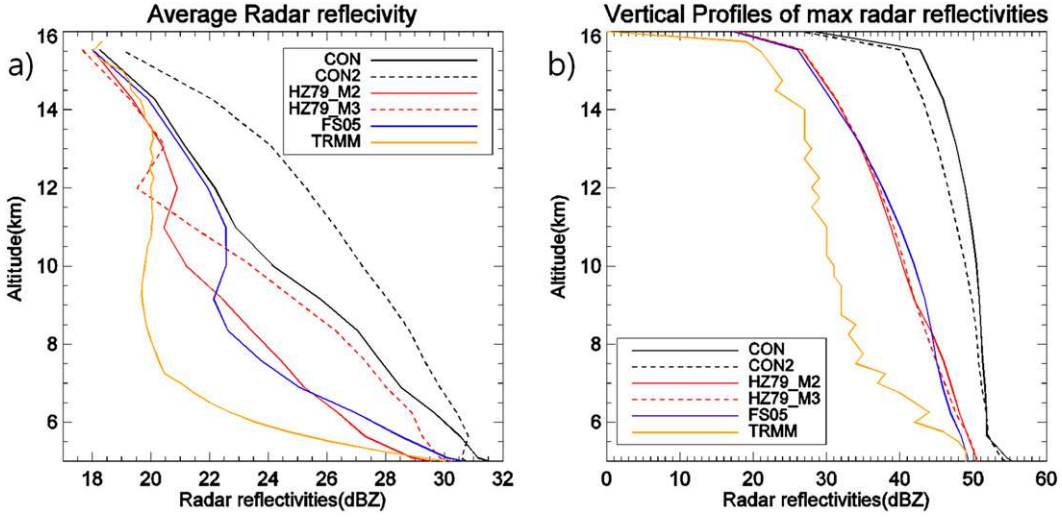

FIG. 8. Comparison of (a) average and (b) maximum radar reflectivity profiles for the parameterizations of snow size distribution. Size distribution assumptions of other precipitating hydrometers are the same in NSW6.

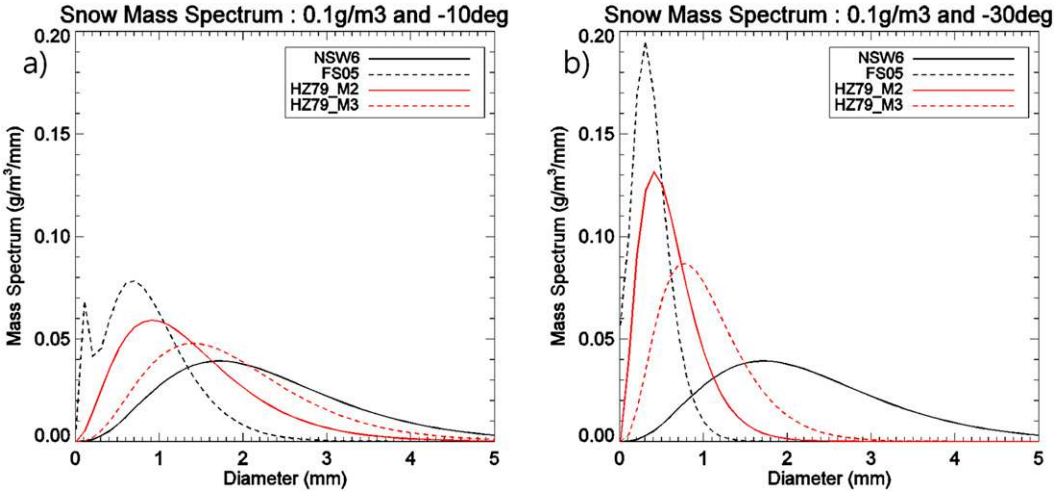

FIG. 9. Snow mass spectrum for the parameterizations of snow size distribution. The ice water content of snow is $0.1\,\mathrm{g\,m^{-3}}$. Air temperatures are (a) −10° and (b) −30°C.

radar reflectivity of the CFADs above the melting layer (Fig. 10). The sensitivity test using high N_{0g} values exhibits a reduced maximum radar reflectivity. The *M–D* relationship affects the vertical profiles of the maximum radar reflectivity. Sensitivity tests for lump graupel in Locatelli and Hobbs (1974) underestimate the average and maximum radar reflectivity above an altitude of 9 km (LG1 and LG100). The third order of the *M–D* relationship of graupel has a vertical profile similar to that of the radar reflectivity in this case (G100). The small graupel size improves vertical profiles of radar reflectivity, whereas the lump graupel assumption reproduces weaker radar reflectivity with lower density than a constant-density assumption over the upper altitude in the convective core.

e. Sensitivity to rain size distribution

The sensitivities to the rain size distributions are examined with the improved snow size distribution in FS05 and graupel size distribution in G100. We test three parameterizations of the rain size distributions: the MP relation with fixed N_{0r}, ZH08, and Combined.

We examine the contribution of each cloud type in the joint histogram as classified in Table 1 as the effects of the rain distribution. The results of the sensitivity experiments are summarized in Table 3, which shows the

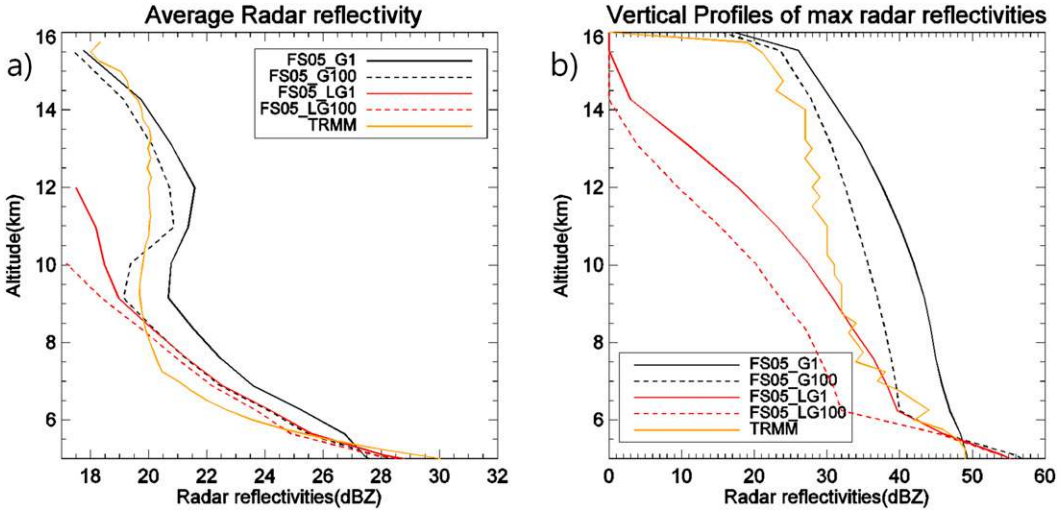

FIG. 10. Comparison of (a) average and (b) maximum radar reflectivity profiles for the parameterizations of graupel size distribution. Snow size distribution is FS05, and other size distribution assumptions are the same in NSW6.

TABLE 3. Frequencies (%) of cloud types for sensitivity experiments on rain size distribution.

Experiment	Shallow	Congestus	Midcold	Deep
TRMM	16.1	14.3	29.9	21.1
CON	37.0	17.7	11.2	21.0
CON2	20.5	9.4	7.8	50.8
FS05_G100_MP	30.7	14.1	16.7	23.8
FS05_G100_ZH08	38.5	12.4	14.3	16.1
FS05_G100_Combined	25.2	16.4	22.9	18.8

ratio of the four categories of cloud types. The MP relation underestimates the midcold clouds compared to the TRMM observation. ZH08 overestimates the shallow clouds and underestimates the deep clouds. Combined increases the midcold clouds compared to MP and decreases shallow clouds compared to ZH08. From CON2 to Combined, the percentage of midcold clouds increases from 7.8% to 22.9%, and the percentage of deep clouds decreases from 50.8% to 18.8%. These values are close to the 29.9% of midcold clouds and 21.1% of deep clouds in the TRMM observation because the rain size of stratiform precipitations is underestimated in the model compared to that of the observation. When the different rain size distribution approach is used, radar reflectivity in the midcold clouds would increase.

The average and maximum radar reflectivities above 10 km are reduced (Fig. 11). We speculate larger rain size distributions with the same liquid water content of ZH08 have the weaker cold pool strengths in stratiform precipitations. This is related to the lower evaporation term in ZH08 near the surface, which produces weaker convection than MP (Li et al. 2009). ZH08 produces faster terminal velocities of rain and reduction of the upper mass flux of rain and graupel produced by freezing of rain compared to MP.

f. Summary of total modifications

We examined how the modifications of the size distributions of snow, graupel, and rain affect the joint histograms and CFADs of deep clouds. The control experiment (CON) with the original scheme NSW6 overestimated radar reflectivity because the temperature dependency of aggregation and the depositional growth of snow are not considered. FS05 improves the joint histogram's bias and CFADs of deep clouds by introducing the temperature dependency of the intercept parameter, the bimodal size distribution, and the second order of the M–D relationship ($\sim D^2$). For graupel, the intercept parameter N_{0g} and the M–D relationship affect the average and maximum radar reflectivities. When the high N_{0g} is introduced based on Knight et al. (1982), better CFAD profiles are reproduced due to a reduction of radar reflectivities in the convective core. The different rain size distribution approach reproduces a realistic fraction of midcold clouds due to increased radar reflectivities in the stratiform precipitation.

We compare the joint histograms of the control experiment and the experiment with the modified size distributions of the three precipitating hydrometeors (combined in section 4d). This experiment is based on FS05 for snow and G100 for graupel. We think that these choices for size distributions are most suitable for experimentation in terms of the joint histograms and

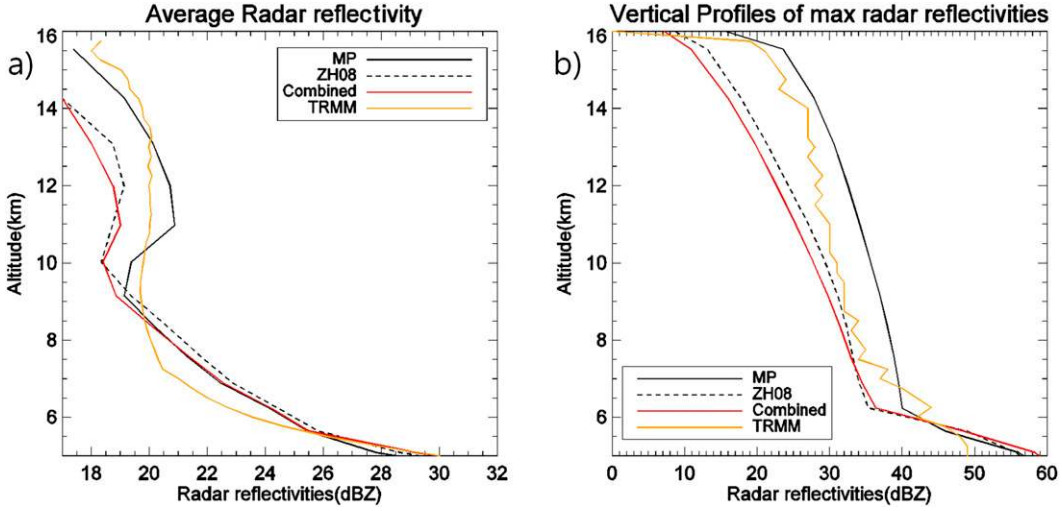

FIG. 11. Comparison of (a) average and (b) maximum radar reflectivity profiles for the parameterizations of rain size distribution. Snow size distribution is FS05; the graupel is G100.

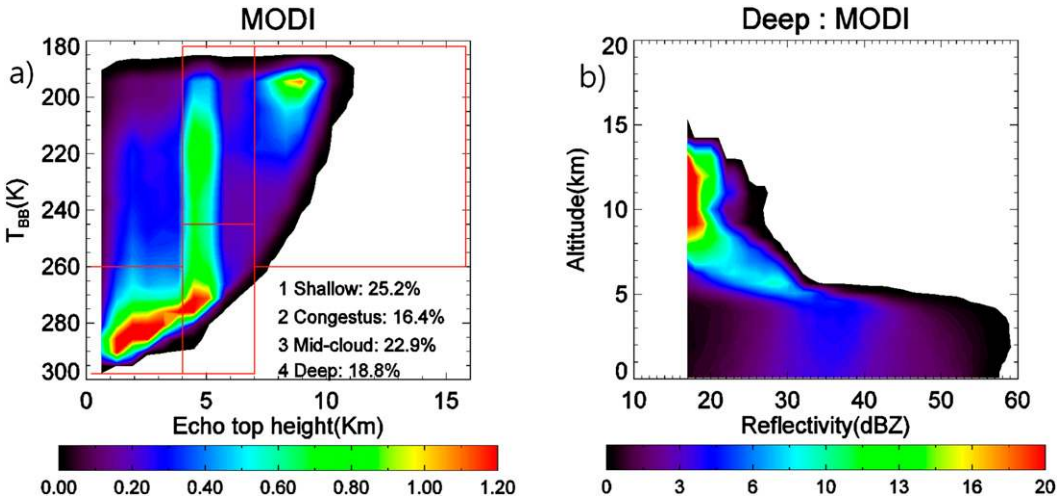

FIG. 12. (a) Joint histograms of PTH and TBB and (b) CFAD of deep clouds of MODI.

CFADs. Hereafter, we referred to this set of size distributions as MODI. As shown in Fig. 12, MODI exhibits reduced PTH height of high frequencies of deep clouds, and the ratio of midcold clouds is increased near the melting layer. The mean radar reflectivity and maximum radar reflectivity in the CFADs of deep clouds are similar to those of the TRMM observations (Figs. 3 and 12). In addition, PTH is reduced in the layers between 5 and 10 km.

The radar reflectivities below the melting level (5 km) are still overestimated, similar to CON. This indicates that the numerical simulation overestimates precipitation, or the MP relation and ZH08 overestimate the radar reflectivity of rain compared with the observations in Tokay and Short (1996) (Fig. 5). Figure 13 corresponds to Fig. 12a and shows that modified size distributions decrease the high frequency of PTH over 10 km and increase frequency near 5 km. The result of MODI is better than that of CON2 for deep clouds and midcold clouds. However, the frequency of PTH is still underestimated between altitudes of 5 and 7 km in the modified run. Figure 14 shows the 7-day-averaged precipitation (mm h^{-1}) among TRMM 3B42, CON, CON2, and MODI. The precipitation is concentrated near 5° latitude in TRMM 3B42 observation. However, CON did not capture the precipitation distribution. The more increased and widespread snow in CON2 make larger stratiform precipitation and the more well-organized mesoscale convective systems than CON. CON2 and MODI reproduce similar precipitation patterns. This indicates that the different precipitating hydrometeors' size distributions do not affect the accumulated precipitation distribution compared to CON2.

5. Discussion

In the previous sections, we improved the results based on TRMM using sensitivity tests of microphysics. We investigate the effects of microphysics on dynamics, domain average temperature, and OLR in this part.

The modification of microphysics affects the dynamics, particularly for vertical wind distribution at upper altitudes. Figure 15a shows the probability distribution of vertical velocity at 10-km altitude. MODI has a relatively high frequency of strong updraft velocity, over 15 m s^{-1} more than that of CON and CON2. We

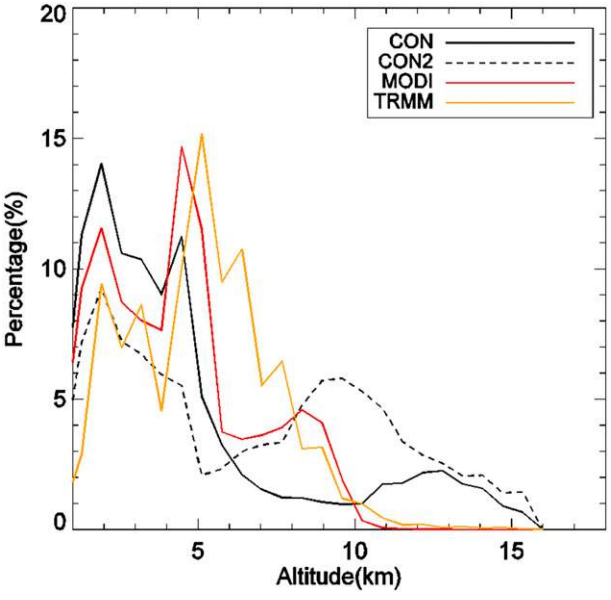

FIG. 13. Comparison of the probability of PTH for the TRMM observation, CON, CON2, and MODI.

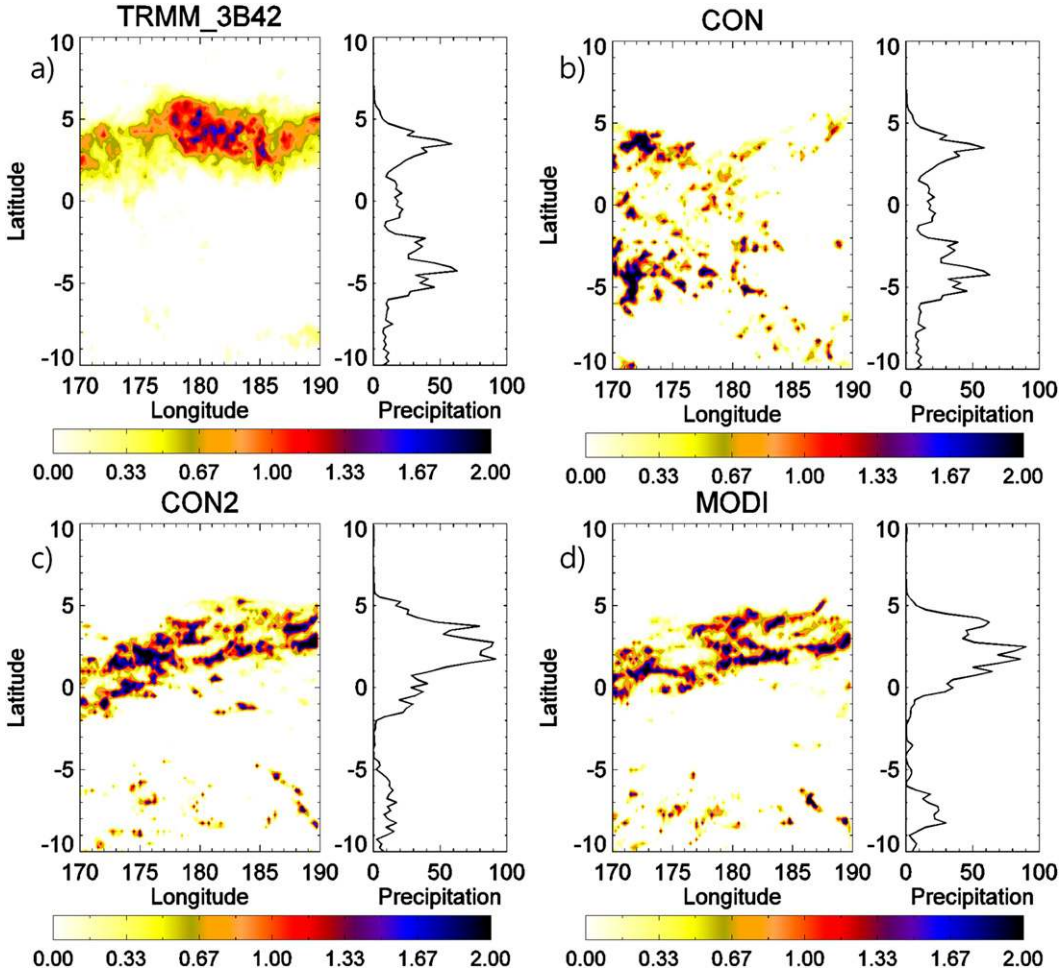

FIG. 14. Comparison of 7-day-averaged precipitation (mm h^{-1}) of (a) TRMM 3B42, (b) CON, (c) CON2, and (d) MODI over the domain.

speculate that this is related to the weakening of precipitation flux with reduced graupel and smaller snow size. These effects are more dominant at altitudes near 10 km than at lower levels.

Vertical profiles of the domain-average temperature between MODI and CON are different (Fig. 15b). The ice nucleation and reduction of graupel has strong effects on the average vertical profile of temperature, which is related to the deposition and sublimation process of snow in CON2. Condensation heating is larger above 10 km because of high relative humidity with respect to ice and abundant snow, whereas sublimation cooling is larger than CON near 6 km.

We compare the domain- and temporal-averaged OLR in the analysis domain among CON, CON2, MODI, and daily National Oceanic and Atmospheric Administration (NOAA) OLR for 7 days (Table 4). This shows that OLR is reduced by more than 15 W m^{-2} in CON2 and MODI compared to that in CON, and it becomes closer to the observation because of the nucleation and reduction of graupel. CON is similar to the result of Blossey et al. (2007) in the overestimation of OLR in cloud-resolving model simulations than observation in KWAJEX. The modified size distributions result in a decrease of approximately 4 W m^{-2} OLR than that produced by CON2. The decrease is related to the snow size distribution parameterization; that is, smaller snow size has more residence time in FS05 than a constant N_{0s}.

We investigated the average ratio of convective to stratiform precipitation (Table 5). We defined mesoscale convective precipitation systems as larger 1225-km^2 rainy areas with over 1 mm h^{-1} precipitation. We divided convective and stratiform precipitation regions using a specific rain rate; the areas over 20 mm h^{-1} were considered as convective precipitation and all other were as stratiform precipitation. The average ratio of convective to stratiform precipitation is reduced from

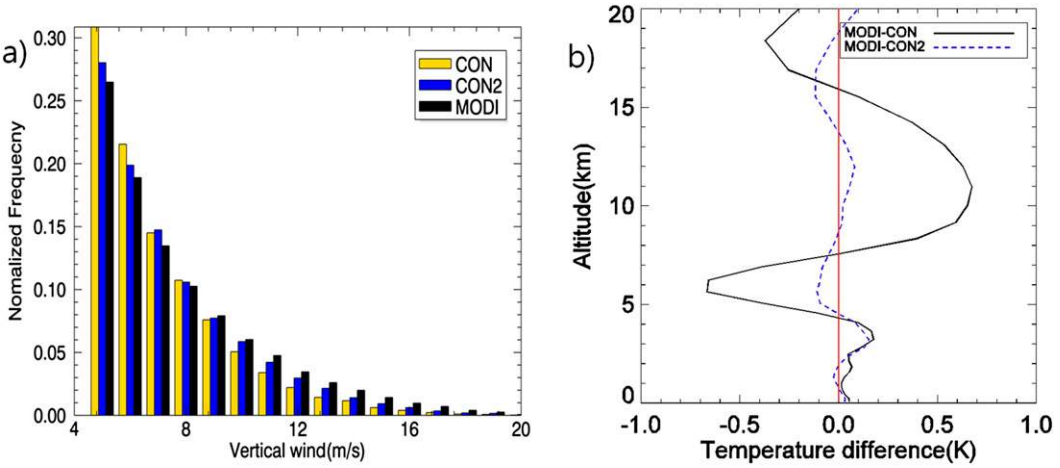

FIG. 15. (a) Normalized frequency of vertical winds for the CON, CON2, and MODI and (b) vertical profiles of averaged temperature differences of MODI with CON and CON2.

24.1% by CON2 to 21.5% by MODI, which indicates that stratiform precipitation increases in MODI.

6. Conclusions

In this study, we evaluated the cloud and precipitation properties of numerical simulations of NICAM for a single-moment bulk microphysics scheme using TRMM PR and TBB with a satellite simulator. We investigated the effect of modifications of the size distributions of precipitating hydrometeors on the joint histogram of TBB and PTH from TRMM PR for mesoscale convective systems over the tropical Pacific Ocean. Cloud system–resolving simulations reproduced a horizontal cloud size distribution similar to those observed by geostationary satellites. We found that the control experiment with the default parameters of NSW6 leads to an overestimated frequency of deep cloud. In other words, the joint histogram analysis shows that the frequency of the deep cloud category is overestimated and that PTH is overestimated above 12 km in the control run, which also underestimates the frequency of midcold clouds.

To improve the statistical frequency and CFADs of the simulated clouds, we examined the effects of hydrometeor size distributions. First, the snow size distribution sensitivity was examined using several *M–D* relationships. Snow size distribution affects the probability distributions of PTH in deep clouds. When the scheme proposed by FS05 is used, the bias from an extensively high PTH is reduced, and the probability of PTH becomes closer to that of the TRMM observation. This is related to the bimodal size distribution and the *M–D* relationship, the latter of which affects the mean radar reflectivity of the CFADs.

Next, we found that graupel size distribution affects the maximum radar reflectivity, which decreased rapidly in the upper troposphere on applying the *M–D* relationship of lump graupel described in Locatelli and Hobbs (1974).

Third, from the sensitivity to rain size distributions, we found that the frequency of shallow, congestus, and midcold clouds could be modified. The ZH08 method reproduces a better representation of stratiform precipitation size distribution. However, the frequency of shallow clouds is increased. Therefore, we introduced a combined parameterization that uses different rain size distributions for convective and stratiform precipitation. Results showed that this parameterization quantitatively improves the frequency of cloud categories in the joint histogram. However, there are overestimations of radar reflectivities below an altitude of 5 km. One possible reason for this is the horizontal resolution: we used a grid space of approximately 3 km for the simulation. Vertical mass flux is overestimated around this resolution because of the underestimation of detrainment (Bryan and Morrison 2012; Caine et al. 2013; Van Weverberg et al. 2013). Another reason might be related to autoconversion and the liquid accretion process; similar overestimation of radar reflectivities is seen in congestus and shallow clouds.

We examined the effect of microphysics on the other cloud properties. The modified microphysics improves

TABLE 4. Domain and temporal averages of OLR ($W m^{-2}$) for 7 days among CON, CON2, MODI, and daily NOAA OLR.

Experiment	CON	CON2	MODI	NOAA OLR
OLR	257.4	242.9	239.1	239.6

TABLE 5. Average ratio (%) of convective to stratiform precipitation among CON, CON2, and MODI.

Experiment	CON	CON2	MODI
Ratio	26.8	24.1	21.5

the accumulated precipitation distribution and domain-averaged OLR for 7 days compared to observations. It increases frequencies of vertical velocities over 15 m s^{-1} at 10-km altitude. The vertical profiles of averaged temperature are changed over the melting layer. The ratio of stratiform precipitation increase in the modified microphysics.

There are more advanced microphysics schemes, such as multimoment or bin microphysics schemes, that reproduce diverse size distributions. However, to interpret the results of such advanced schemes compared to satellite data, we need to understand how hydrometeor size distribution affects radiances from the cloud properties in numerical simulations. In fact, we found that the parameters assumed in the single-moment microphysical scheme control the cloud and precipitation properties. According to this study, the parameterization of the snow size distribution, which is affected by the aggregation–autoconversion processes, is related to the distributions of the frequencies of deep clouds in the joint histogram. The *M–D* relationship for snow affects the average radar reflectivity of the CFADs in deep clouds. The maximum radar reflectivity is affected by riming and the graupel density. On the basis of the results shown here, we will be able to analyze the results of other advanced microphysical schemes using the joint histogram framework with the single-moment bulk microphysics scheme. In addition, because the diagnostic relationships for the size distributions used in this study are based on observations, the size distributions of other schemes should be checked using these relationships. Comparisons of microphysics schemes of differing complexity will reveal further important factors in the size distributions using the methods proposed in this study.

In this study, we focused on the central Pacific and obtained better results for joint histograms, CFADs, and OLR compared to observations. Microphysical characteristics vary in different locations of all oceans. In the future, we intend to expand the global simulation to include evaluations using a several-kilometer homogenous resolution to assess these modifications in all oceans. We also intend to perform comparisons using data from other satellites, such as *CloudSat* and *CALIPSO*.

Acknowledgments. We thank Dr. T. Hashino, Dr. N. Kuba, and Dr. T. Inoue for helpful discussions. We thank Dr. H. Masunaga of Nagoya University for the use of the SDSU. TRMM data were obtained from NASA and the Japan Aerospace Exploration Agency. *MTSAT* data were provided by the Meteorological Research Institute. Simulations were performed using the HITACHI SR16000 at the Information Technology Center, University of Tokyo. This research was supported by the High Performance Computing Infrastructure Strategic Program, the Core Research for Evolutional Science and Technology Program of the Japan Science and Technology Agency, and the Innovative Program of Climate Change Projection for the 21st Century Project funded by the Ministry of Education, Culture, Sports, Science, and Technology, Japan.

REFERENCES

Blossey, P. N., C. S. Bretherton, J. Cetrone, and M. Kharoutdinov, 2007: Cloud-resolving model simulations of KWAJEX: Model sensitivities and comparisons with satellite and radar observations. *J. Atmos. Sci.,* **64,** 1488–1508, doi:10.1175/JAS3982.1.

Bodas-Salcedo, A., and Coauthors, 2011: COSP: Satellite simulation software for model assessment. *Bull. Amer. Meteor. Soc.,* **92,** 1023–1043, doi:10.1175/2011BAMS2856.1.

Bohren, C. F., and L. J. Battan, 1982: Radar backscattering of microwaves by spongy ice spheres. *J. Atmos. Sci.,* **39,** 2623–2628, doi:10.1175/1520-0469(1982)039<2623:RBOMBS>2.0.CO;2.

Bryan, G. H., and H. Morrison, 2012: Sensitivity of a simulated squall line to horizontal resolution and parameterization of microphysics. *Mon. Wea. Rev.,* **140,** 202–225, doi:10.1175/MWR-D-11-00046.1.

Caine, S., T. P. Lane, P. T. May, C. Jakob, S. T. Siems, M. J. Manton, and J. Pinto, 2013: Statistical assessment of tropical convection-permitting model simulations using a cell-tracking algorithm. *Mon. Wea. Rev.,* **141,** 557–581, doi:10.1175/MWR-D-11-00274.1.

Delanoe, J., R. J. Hogan, R. M. Forbes, A. Bodas-Salcedo, and T. H. M. Stein, 2011: Evaluation of ice cloud representation in the ECMWF and UK Met Office models using CloudSat and CALIPSO data. *Quart. J. Roy. Meteor. Soc.,* **137,** 2064–2078, doi:10.1002/qj.882.

Fabry, F., and W. Szyrmer, 1999: Modeling of the melting layer. Part II: Electromagnetic. *J. Atmos. Sci.,* **56,** 3593–3600, doi:10.1175/1520-0469(1999)056<3593:MOTMLP>2.0.CO;2.

Field, P. R., R. J. Hogan, P. R. A. Brown, A. J. Illingworth, T. W. Choularton, and R. J. Cotton, 2005: Parametrization of ice-particle size distributions for mid-latitude stratiform cloud. *Quart. J. Roy. Meteor. Soc.,* **131,** 1997–2017, doi:10.1256/qj.04.134.

Gilmore, M. S., J. M. Straka, and E. N. Rasmussen, 2004: Precipitation uncertainty due to variations in precipitation particle parameters within a simple microphysics scheme. *Mon. Wea. Rev.,* **132,** 2610–2627, doi:10.1175/MWR2810.1.

Gunn, K. L. S., and J. S. Marshall, 1958: The distribution with size of aggregate snowflakes. *J. Meteor.,* **15,** 452–461, doi:10.1175/1520-0469(1958)015<0452:TDWSOA>2.0.CO;2.

Hashino, T., M. Satoh, Y. Hagihara, T. Kubota, T. Matsui, T. Nasuno, and H. Okamoto, 2013: Evaluating cloud microphysics from NICAM against CloudSat and CALIPSO. *J. Geophys. Res. Atmos.,* **118,** 7273–7292, doi:10.1002/jgrd.50564.

Heymsfield, A. J., P. Field, and A. Bansemer, 2008: Exponential size distributions for snow. *J. Atmos. Sci.,* **65,** 4017–4031, doi:10.1175/2008JAS2583.1.

Hong, S.-Y., J. Dudhia, and S.-H. Chen, 2004: A revised approach to ice microphysical processes for the bulk parameterization of clouds and precipitation. *Mon. Wea. Rev.,* **132,** 103–120, doi:10.1175/1520-0493(2004)132<0103:ARATIM>2.0.CO;2.

——, K. S. S. Lim, Y. H. Lee, J. C. Ha, H. W. Kim, S. J. Ham, and J. Dudhia, 2010: Evaluation of the WRF double-moment 6-class microphysics scheme for precipitating convection. *Adv. Meteor.,* 2010, 707253, doi:10.1155/2010/707253.

Houze, R. A., P. V. Hobbs, P. H. Herzegh, and D. B. Parsons, 1979: Size distributions of precipitation particles in frontal clouds. *J. Atmos. Sci.,* **36,** 156–162, doi:10.1175/1520-0469(1979)036<0156:SDOPPI>2.0.CO;2.

Iguchi, T., T. Nakajima, A. P. Khain, K. Saito, T. Takemura, and K. Suzuki, 2008: Modeling the influence of aerosols on cloud microphysical properties in the East Asia region using a mesoscale model coupled with a bin-based cloud microphysics scheme. *J. Geophys. Res.,* **113,** D14215, doi:10.1029/2007JD009774.

Inoue, T., M. Satoh, H. Miura, and B. Mapes, 2008: Characteristics of cloud size of deep convection simulated by a global cloud resolving model over the western tropical Pacific. *J. Meteor. Soc. Japan,* **86A,** 1–15, doi:10.2151/jmsj.86A.1.

——, ——, Y. Hagihara, H. Miura, and J. Schmetz, 2010: Comparison of high-level clouds represented in a global cloud system–resolving model with CALIPSO/CloudSat and geostationary satellite observations. *J. Geophys. Res.,* **115,** D00H22, doi:10.1029/2009JD012371.

Janowiak, J. E., R. J. Joyce, and Y. Yarosh, 2001: A real-time global half-hourly pixel-resolution infrared dataset and its applications. *Bull. Amer. Meteor. Soc.,* **82,** 205–217, doi:10.1175/1520-0477(2001)082<0205:ARTGHH>2.3.CO;2.

Khain, A., and B. Lynn, 2009: Simulation of a supercell storm in clean and dirty atmosphere using weather research and forecast model with spectral bin microphysics. *J. Geophys. Res.,* **114,** D19209, doi:10.1029/2009JD011827.

Knight, C. A., W. A. Cooper, I. R. Breed, I. R. Paluch, P. L. Smith, and G. Vali, 1982: *Microphysics.* Vol. 1. Colorado Associated University Press (in association with the National Center for Atmospheric Research), 282 pp.

Kodama, C., A. T. Noda, and M. Satoh, 2012: An assessment of the cloud signals simulated by NICAM using ISCCP, CALIPSO, and CloudSat satellite simulators. *J. Geophys. Res.,* **117,** D12210, doi:10.1029/2011JD017317.

Lang, S. E., W.-K. Tao, R. Cifelli, W. Olson, J. Halverson, S. Rutledge, and J. Simpson, 2007: Improving simulations of convective systems from TRMM LBA: Easterly and westerly regimes. *J. Atmos. Sci.,* **64,** 1141–1164, doi:10.1175/JAS3879.1.

——, ——, X. Zeng, and Y. Li, 2011: Reducing the biases in simulated radar reflectivities from a bulk microphysics scheme: Tropical convective systems. *J. Atmos. Sci.,* **68,** 2306–2320, doi:10.1175/JAS-D-10-05000.1.

Li, X., W.-K. Tao, A. P. Khain, J. Simpson, and D. E. Johnson, 2009: Sensitivity of a cloud-resolving model to bulk and explicit bin microphysical schemes. Part II: Cloud microphysics and storm dynamics interactions. *J. Atmos. Sci.,* **66,** 22–40, doi:10.1175/2008JAS2647.1.

Li, Y., E. J. Zipser, S. K. Krueger, and M. A. Zulauf, 2008: Cloud-resolving modeling of deep convection during KWAJEX. Part I: Comparison to TRMM satellite and ground-based radar observations. *Mon. Wea. Rev.,* **136,** 2699–2712, doi:10.1175/2007MWR2258.1.

Lim, K.-S. S., and S.-Y. Hong, 2010: Development of an effective double-moment cloud microphysics scheme with prognostic cloud condensation nuclei (CCN) for weather and climate models. *Mon. Wea. Rev.,* **138,** 1587–1612, doi:10.1175/2009MWR2968.1.

Lin, Y., and B. A. Colle, 2011: A new bulk microphysical scheme that includes riming intensity and temperature-dependent ice characteristics. *Mon. Wea. Rev.,* **139,** 1013–1035, doi:10.1175/2010MWR3293.1.

Lin, Y.-L., R. D. Farley, and H. D. Orville, 1983: Bulk parameterization of the snow field in a cloud model. *J. Climate Appl. Meteor.,* **22,** 1065–1092, doi:10.1175/1520-0450(1983)022<1065:BPOTSF>2.0.CO;2.

Locatelli, J. D., and P. V. Hobbs, 1974: Fall speeds and masses of solid precipitation particles. *J. Geophys. Res.,* **79,** 2185–2197, doi:10.1029/JC079i015p02185.

Luo, Y., Y. Wang, H. Wang, Y. Zheng, and H. Morrison, 2010: Modeling convective-stratiform precipitation processes on a mei-yu front with the Weather Research and Forecasting model: Comparison with observations and sensitivity to cloud microphysics parameterizations. *J. Geophys. Res.,* **115,** D18117, doi:10.1029/2010JD013873.

Lynn, B. H., A. P. Khain, J. Dudhia, D. Rosenfeld, A. Pokrovsky, and A. Seifert, 2005: Spectral (bin) microphysics coupled with a mesoscale model (MM5). Part I: Model description and first results. *Mon. Wea. Rev.,* **133,** 44–58, doi:10.1175/MWR-2840.1.

Maki, M., T. D. Keenan, Y. Sasaki, and K. Nakamura, 2001: Characteristics of the raindrop size distribution in tropical continental squall lines observed in Darwin, Australia. *J. Appl. Meteor.,* **40,** 1393–1412, doi:10.1175/1520-0450(2001)040<1393:COTRSD>2.0.CO;2.

Marshall, J. S., and W. M. Palmer, 1948: The distribution of raindrops with size. *J. Meteor.,* **5,** 165–166, doi:10.1175/1520-0469(1948)005<0165:TDORWS>2.0.CO;2.

Masunaga, H., and C. D. Kummerow, 2006: Observations of tropical precipitating clouds ranging from shallow to deep convective systems. *Geophys. Res. Lett.,* **33,** L16805, doi:10.1029/2006GL026547.

——, M. Satoh, and H. Miura, 2008: A joint satellite and global cloud-resolving model analysis of a Madden-Julian oscillation event: Model diagnosis. *J. Geophys. Res.,* **113,** D17210, doi:10.1029/2008JD009986.

——, and Coauthors, 2010: Satellite data simulator unit: A multisensor, multispectral satellite simulator package. *Bull. Amer. Meteor. Soc.,* **91,** 1625–1632, doi:10.1175/2010BAMS2809.1.

Matrosov, S. Y., 1992: Radar reflectivity in snowfall. *IEEE Trans. Geosci. Remote Sens.,* **30,** 454–461, doi:10.1109/36.142923.

Matsui, T., X. Zeng, W.-K. Tao, H. Masunaga, W. S. Olson, and S. Lang, 2009: Evaluation of long-term cloud-resolving model simulations using satellite radiance observations and multifrequency satellite simulators. *J. Atmos. Oceanic Technol.,* **26,** 1261–1274, doi:10.1175/2008JTECHA1168.1.

Maxwell Garnett, J. C., 1904: Colours in metal glasses and metal films. *Philos. Trans. Roy. Soc. London,* **A203,** 385–420, doi:10.1098/rsta.1904.0024.

Milbrandt, J. A., and M. K. Yau, 2005: A multimoment bulk microphysics parameterization. Part II: A proposed three-moment closure and scheme description. *J. Atmos. Sci.,* **62,** 3065–3081, doi:10.1175/JAS3535.1.

——, ——, J. Mailhot, and S. Belair, 2008: Simulation of an orographic precipitation event during IMPROVE-2. Part I: Evaluation of the control run using a triple-moment bulk microphysics scheme. *Mon. Wea. Rev.,* **136,** 3873–3893, doi:10.1175/2008MWR2197.1.

Miura, H., M. Satoh, T. Nasuno, A. T. Noda, and K. Oouchi, 2007: A Madden-Julian oscillation event realistically simulated by a global cloud-resolving model. *Science,* **318,** 1763–1765, doi:10.1126/science.1148443.

Molthan, A. L., W. A. Petersen, S. W. Nesbitt, and D. Hudak, 2010: Evaluating the snow crystal size distribution and density assumptions within a single-moment microphysics scheme. *Mon. Wea. Rev.,* **138,** 4254–4267, doi:10.1175/2010MWR3485.1.

Morrison, H., J. A. Curry, and V. I. Khvorostyanov, 2005: A new double-moment microphysics parameterization for application in cloud and climate models. Part I: Description. *J. Atmos. Sci.,* **62,** 1665–1677, doi:10.1175/JAS3446.1.

——, G. Thompson, and V. Tatarskii, 2009: Impact of cloud microphysics on the development of trailing stratiform precipitation in a simulated squall line: Comparison of one- and two-moment schemes. *Mon. Wea. Rev.,* **137,** 991–1007, doi:10.1175/2008MWR2556.1.

NCEP, cited 2011: NCEP FNL operational model global tropospheric analyses, continuing from July 1999. Research Data Archive at the National Center for Atmospheric Research, Computational and Information Systems Laboratory, Boulder, CO. [Available online at http://rda.ucar.edu/datasets/ds083.2.]

Powell, S. W., R. A. Houze, A. Kumar, and S. A. McFarlane, 2012: Comparison of simulated and observed continental tropical anvil clouds and their radiative heating profiles. *J. Atmos. Sci.,* **69,** 2662–2681, doi:10.1175/JAS-D-11-0251.1.

Rao, T. N., D. N. Rao, K. Mohan, and S. Raghavan, 2001: Classification of tropical precipitating systems and associated *Z-R* relationships. *J. Geophys. Res.,* **106,** 17 699–17 711, doi:10.1029/2000JD900836.

Rutledge, S. A., and P. V. Hobbs, 1984: The mesoscale and microscale structure and organization of clouds and precipitation in midlatitude cyclones. XII: A diagnostic modeling study of precipitation development in narrow cold-frontal rainbands. *J. Atmos. Sci.,* **41,** 2949–2972, doi:10.1175/1520-0469(1984)041<2949:TMAMSA>2.0.CO;2.

Satoh, M., and Y. Matsuda, 2009: Statistics on high-cloud areas and their sensitivities to cloud microphysics using single-cloud experiments. *J. Atmos. Sci.,* **66,** 2659–2677, doi:10.1175/2009JAS2948.1.

——, T. Matsuno, H. Tomita, H. Miura, T. Nasuno, and S. Iga, 2008: Nonhydrostatic Icosahedral Atmospheric Model (NICAM) for global cloud resolving simulations. *J. Comput. Phys.,* **227,** 3486–3514, doi:10.1016/j.jcp.2007.02.006.

——, T. Inoue, and H. Miura, 2010: Evaluations of cloud properties of global and local cloud system resolving models using CALIPSO and CloudSat simulators. *J. Geophys. Res.,* **115,** D00H14, doi:10.1029/2009JD012247.

Seifert, A., and K. D. Beheng, 2006: A two-moment cloud microphysics parameterization for mixed-phase clouds. Part 1: Model description. *Meteor. Atmos. Phys.,* **92,** 45–66, doi:10.1007/s00703-005-0112-4.

Seiki, T., and T. Nakajima, 2014: Aerosol effects of the condensation process on a convective cloud simulation. *J. Atmos. Sci.,* 71, 833–853, doi:10.1175/JAS-D-12-0195.1.

——, M. Satoh, H. Tomita, and T. Nakajima, 2014: Simultaneous evaluation of ice cloud microphysics and non-sphericity of the cloud optical properties using hydrometeor video sonde and radiometer sonde in-situ observations. *J. Geophys. Res.,* doi:10.1002/2013JD021086, in press.

Stith, J. L., J. E. Dye, A. Bansemer, A. J. Heymsfield, C. A. Grainger, W. A. Petersen, and R. Cifelli, 2002: Microphysical observations of tropical clouds. *J. Appl. Meteor.,* **41,** 97–117, doi:10.1175/1520-0450(2002)041<0097:MOOTC>2.0.CO;2.

Suzuki, K., T. Nakajima, T. Y. Nakajima, and A. P. Khain, 2010: A study of microphysical mechanisms for correlation patterns between droplet radius and optical thickness of warm clouds with a spectral bin microphysics cloud model. *J. Atmos. Sci.,* **67,** 1126–1141, doi:10.1175/2009JAS3283.1.

Tao, W. K., J. Simpson, and M. McCumber, 1989: An ice water saturation adjustment. *Mon. Wea. Rev.,* **117,** 231–235, doi:10.1175/1520-0493(1989)117<0231:AIWSA>2.0.CO;2.

Thompson, G., P. R. Field, R. M. Rasmussen, and W. D. Hall, 2008: Explicit forecasts of winter precipitation using an improved bulk microphysics scheme. Part II: Implementation of a new snow parameterization. *Mon. Wea. Rev.,* **136,** 5095–5115, doi:10.1175/2008MWR2387.1.

Tokay, A., and D. A. Short, 1996: Evidence from tropical raindrop spectra of the origin of rain from stratiform versus convective clouds. *J. Appl. Meteor.,* **35,** 355–371, doi:10.1175/1520-0450(1996)035<0355:EFTRSO>2.0.CO;2.

Tomita, H., 2008a: New microphysical schemes with five and six categories by diagnostic generation of cloud ice. *J. Meteor. Soc. Japan,* **86A,** 121–142, doi:10.2151/jmsj.86A.121.

——, 2008b: A stretched icosahedral grid by a new grid transformation. *J. Meteor. Soc. Japan,* **86A,** 107–119, doi:10.2151/jmsj.86A.107.

——, and M. Satoh, 2004: A new dynamical framework of nonhydrostatic global model using the icosahedral grid. *Fluid Dyn. Res.,* **34,** 357–400, doi:10.1016/j.fluiddyn.2004.03.003.

Van Weverberg, K., N. P. M. van Lipzig, and L. Delobbe, 2011: The impact of size distribution assumptions in a bulk one-moment microphysics scheme on simulated surface precipitation and storm dynamics during a low-topped supercell case in Belgium. *Mon. Wea. Rev.,* **139,** 1131–1147, doi:10.1175/2010MWR3481.1.

——, A. M. Vogelmann, H. Morrison, and J. A. Milbrandt, 2012: Sensitivity of idealized squall-line simulations to the level of complexity used in two-moment bulk microphysics schemes. *Mon. Wea. Rev.,* **140,** 1883–1907, doi:10.1175/MWR-D-11-00120.1.

——, and Coauthors, 2013: The role of cloud microphysics parameterization in the simulation of mesoscale convective system clouds and precipitation in the tropical western Pacific. *J. Atmos. Sci.,* **70,** 1104–1128, doi:10.1175/JAS-D-12-0104.1.

Varble, A., and Coauthors, 2011: Evaluation of cloud-resolving model intercomparison simulations using TWP-ICE observations: Precipitation and cloud structure. *J. Geophys. Res.,* **116,** D12206, doi:10.1029/2010JD015180.

Zhang, G., M. Xue, Q. Cao, and D. Dawson, 2008: Diagnosing the intercept parameter for exponential raindrop size distribution based on video disdrometer observations: Model development. *J. Appl. Meteor. Climatol.,* **47,** 2983–2992, doi:10.1175/2008JAMC1876.1.

Zhou, Y. P., and Coauthors, 2007: Use of high-resolution satellite observations to evaluate cloud and precipitation statistics from cloud-resolving model simulations. Part I: South China Sea monsoon experiment. *J. Atmos. Sci.,* **64,** 4309–4329, doi:10.1175/2007JAS2281.1.